

Effect of a collapsing gas bubble on the shock-to-detonation transition in liquid nitromethane

W. D. Turley,¹ B. M. La Lone,^{1,a)} J. G. Mance,¹ M. D. Staska,¹ G. D. Stevens,¹ L. R. Veaser,² T. D. Aslam,³ and D. M. Dattelbaum³

¹⁾*Nevada National Security Sites, Special Technologies Laboratory, Santa Barbara, California 93111, USA*

²⁾*Nevada National Security Sites, Los Alamos Operations, Los Alamos, New Mexico 87544, USA*

³⁾*Los Alamos National Laboratory, Los Alamos, New Mexico 87545, USA*

a) Author to whom correspondence should be addressed: LaloneBM@nv.doe.gov

(Dated: 26 September 2024)

We studied the shock-induced collapse of butane gas bubbles in the homogeneous explosive nitromethane (NM) to investigate effects of hot spot formation on the detonation process. A butane bubble was injected into a sample of NM, and a shock wave from a flat plate impactor compressed the bubble, creating a localized hot spot. We measured shock and detonation wave speeds with optical velocimetry, and we used a high-speed camera to image the shock propagation and bubble collapse processes. A multiband optical fiber pyrometer measured the time-resolved thermal radiance, and we used the results and emissivity values extracted from spectral fits to estimate temperatures. We measured characteristics of the shock-to-detonation transition in NM with and without a bubble. All experiments were performed at shock pressures near 8 GPa, where neat NM can detonate. A single bubble in this system was shown to sensitize the NM, leading to a reduced run-to-detonation time. We used hydrodynamic modeling to predict shock wave propagation, extent of chemical reaction, and subsequent temperature rise from the collapsing bubble. We used a temperature-dependent Arrhenius burn model for simulations, and it yielded much better results than reactive burn models that depend only on pressure and density.

I. INTRODUCTION

Chemical reactions in high explosives (HE) can be initiated by shock wave compression of the unreacted explosive. The mechanism of initiation can differ depending on whether the HE is homogeneous or not. It is believed that initiation in granular explosives can occur in hot spots through the localization of energy because of shock wave interactions with the explosive microstructure. Hot spots can form from compression of voids. In homogeneous HE, such as liquids or single crystals, however, initiation occurs via heating due to shock wave compression of the bulk HE. The energy released in these reactions supports continued shock propagation in the HE and the eventual formation of a detonation wave, where the shock speed and chemical reaction rates reach a steady state (Chaiken 1960; Howe *et al.* 1976; and Handley *et al.* 2018). In this work, we introduced a butane bubble into liquid nitromethane (NM) to create a void, a potential hot spot, and we studied the resulting changes in initiation.

Understanding the role of a void in initiation of an explosive is greatly enhanced if it can be modeled computationally. In the literature, for example, 2D and 3D simulations of void collapse in NM by Michael and Nikiforakis (2019a, 2019b) use a temperature-dependent Arrhenius reaction rate law to model the reactions. They simulated the temperature increase from bubble collapse and the resulting hot spot and used it to predict the rate

and extent of chemical reaction in a shocked explosive.

Numerical simulation of void collapse has few validating experimental studies. The most important is the work of Bourne and colleagues (Bourne and Field 1991, 1999; and Bourne and Milne 2002, 2003), but again, there are few quantitative experimental observations and little temperature data to validate the models.

In this study, we performed a series of experiments to observe void collapse in shock-compressed NM. Butane gas bubbles were injected into neat NM to serve as the seeds for hot spots. We chose NM because it is transparent, suitable for optical imaging, and homogeneous. For these reasons, NM has been used in prior experiments and simulations of void collapse (Michael and Nikiforakis 2019a; and Turley *et al.* 2021). Butane was chosen as the gas because its high molecular weight and low ratio of specific heats result in a relatively low temperature rise upon compression. These features minimize the radiance from the compressed gas. Prior studies have shown that the gas temperature inside a void may reach high values ($>10\,000$ K) (Bourne and Field 1991, 1999; Bourne and Milne 2002, 2003; and Flannigan and Suslick 2005), but the small mass of the gas is believed to keep it from being a dominant effect during hot spot formation. Instead, collision of the explosive with itself as the void collapses is believed to dominate hot spot formation. The bubbles in our work are much larger (0.8×1.4 mm) than realistic voids in, for example, plastic-bonded explosive (PBX). We used this larger bubble size as a starting point to develop methods to diagnose features of the void collapse. With this

approach, a single bubble can be directly compared to simulations with a reasonable computational grid size.

In our prior work (Turley *et al.* 2021), we used a small explosive charge to initiate detonation, added diethylenetriamine sensitizer to the NM to assist detonation, and used helium gas to form bubbles. All of these choices were subsequently identified as experimental limitations. We have improved our approach by replacing helium with butane, eliminating the sensitizer, and using a supported shock from a powder gun impactor instead of the explosive charge to better control the shock state of NM. This experimental approach allows us to image the shocked NM with a high-speed framing camera, and at the same time, measure material velocities, radiance, and spectroscopic signals. In a series of dynamic experiments, we measured four important conditions of shocked NM: NM with and without a bubble, and with and without detonation. With our suite of measurement tools and this experimental approach, we were able to demonstrate the effects of a collapsing bubble on the explosive detonation process.

II. EXPERIMENT SETUP AND OPERATION

All dynamic experiments were performed with a 40 mm bore, single-stage powder gun. In a typical experiment, a 24 mm diameter by 8 mm thick aluminum plate traveling at a velocity of ~ 2.2 km/s exits the gun and impacts a polymethyl methacrylate (PMMA) vessel containing the NM sample. A shock wave is launched into the PMMA and NM, compressing and heating the NM. The experimental setup is shown schematically in Fig. 1. The measured shock parameters are presented in Table I.

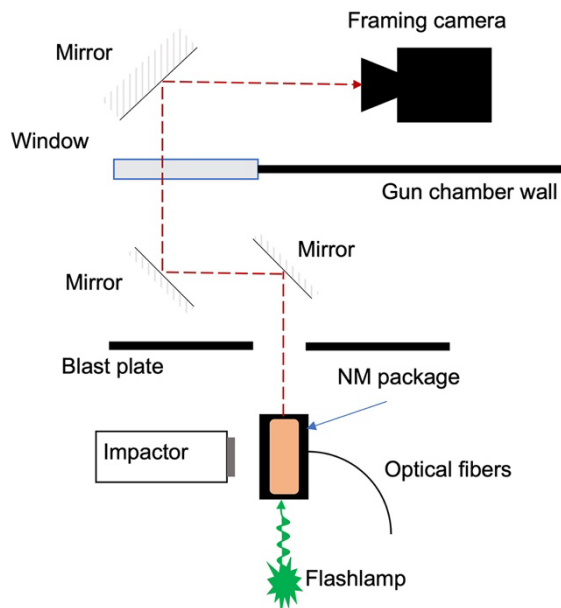


FIG. 1. Schematic view of the NM package illustrating the placement of the visible light framing camera, relay mirrors, expendable flashlamp illuminator, and package location inside the vessel. Optical beam interrupt (OBI) fibers (not shown) send and receive light through the package to trigger the experiment when a rising bubble interrupts the beam. The optical fibers collect velocimetry and radiance signals.

We studied the NM experiments using a fast, visible-light framing camera, time-resolved velocimetry, time-resolved pyrometry, and an optical spectrometer. The experiment package containing the NM, shown in Fig. 2, was made from 3D printed PMMA. The rectangular (38 mm tall \times 12.7 mm deep \times 43 mm wide) package was fitted with borosilicate optical windows for imaging.

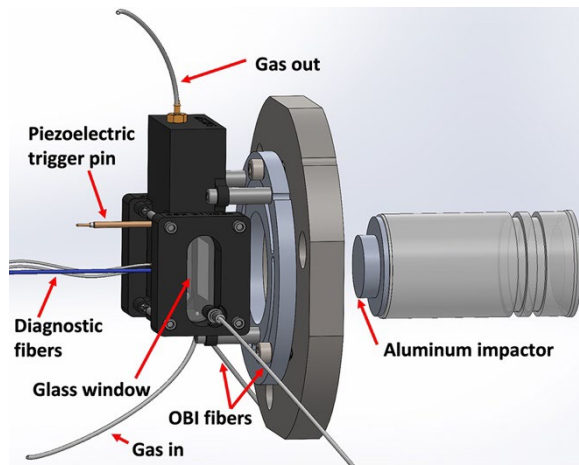


FIG. 2. Rendering of the experimental package mounted on the gun barrel, butane gas inlet and outlet tubes, and PDV and radiance fibers. The optical beam interrupt (OBI) fibers sense the bubble passage and are used for triggering the powder gun after a set delay so that the bubble is in the middle of the package at the time of impact. The piezoelectric pin is used for triggering the framing camera.

The NM was 99.0% reagent plus grade and was used as acquired from Sigma-Aldrich. Its density was 1.127 g/cm^3 . To verify that the NM would not dissolve the 3D printed PMMA, we soaked PMMA overnight in NM; no noticeable effects were observed. Furthermore, all dynamic experiments were executed within an hour of filling the vessel. Once assembled, the package was mounted on an alignment plate at the end of the gun barrel. Xenon flashlamp light was sent into one window, and optical images were collected through the opposite window. Optical fibers inserted into the package were used for photonic Doppler velocimetry (PDV), time-resolved radiance, and spectral measurements. The fibers were mounted at the end of the package, $\sim 11 \text{ mm}$ from the drive surface where the NM shock wave originated.

A stream of butane gas (Airgas, 99.99%) bubbles was fed into the NM from the bottom of the package through a small-aperture ($127 \mu\text{m}$ diameter) needle. The flow rate was adjusted so there would be only one bubble in the NM at the time of the experiment. The capillary tube was positioned at the bottom center of the experiment package, 2 mm from the PMMA wall (see Fig. 2). Given the simplicity of this system, the bubbles were not spherical. Although reproducible, the bubbles were flattened by gravity into oblate spheroids that appear roughly elliptical in shape (typical dimensions $\sim 0.8 \text{ mm}$ high \times 1.4 mm wide) in the 2D framing camera images.

Optical beam interrupt (OBI) fibers were placed on either side of the package. When a rising bubble passes through and interrupts the beam of 1550 nm continuous light between the OBI fibers, a prompt signal is produced. This signal is used as the trigger signal to initiate the gun propellant that launches the impactor. The source and collection OBI fibers were mounted externally onto the package, and the light was sent through the bottom of the package as shown in Fig. 2. Additionally, separate OBI fibers at the end of the gun barrel provided a pre-trigger for the flashlamp illuminator. We also used these gun barrel fibers to measure impactor velocity. A lithium niobate piezoelectric pin mounted in the NM package was used as a trigger for the framing camera to begin capturing images when the impactor strikes the package.

We fielded both collimated (input and reflected light in the same fiber) and two-fiber (separate fibers for input and return) PDV optical probes (AC Photonics) to capture velocimetry signatures. We found signals from the collimated fiber probes to be less reliable than those from the two-fiber probes because of their lower collection efficiency. The two-fiber probes most reliably returned reflected signals from the package interface, shock wave, and detonation wave. We added a $25 \mu\text{m}$ thick aluminum foil to the PMMA surface where the shock enters the NM package to increase reflectivity for the PDV laser from this interface. In this paper we intend *interface* or *package interface* to mean this interface, where the PMMA and its thin aluminum reflecting cover meet NM.

To derive true shock velocities requires the as-measured, or apparent, shock wave velocities in NM to

be divided by the ambient NM refractive index, n_0 . From the corrected velocities we can estimate pressures and other continuum properties. Mercier *et al.* (2010) report using $n_0 = 1.368$ for detonating NM, but we were unable to find a measured literature value for the ambient refractive index of NM at wavelengths near 1550 nm . Using spectral interferometry on a static 1 cm path length of NM, we determined the group refractive index to be $n_0 = 1.376$, and we used this value to estimate the shock velocities shown in Table I. (It is reasonable to expect that using the group refractive index instead of the ambient refractive index results in only a small velocity error.) In many cases, the PDV spectrograms showed sufficient signals from both the package interface and the shock front to allow useful velocity measurements during the experiments. We calculated interface particle velocities and pressures using the measured shock velocities at breakout and the NM shock velocity vs particle velocity equation of state (EOS) relationship given by Winey *et al.* (2000): $U_{shock} = 1.66 + 1.637 U_{particle}$. (This EOS assumes that the sound speed is $c = 1.33 \text{ km/s}$ at $20 \text{ }^\circ\text{C}$; see Lysne and Hardesty 1973.) However, when we did not resolve shock or detonation velocities, we used the gun barrel OBI signals to calculate the aluminum impactor velocity, and the known EOS of PMMA and aluminum to calculate the package interface velocity. Using this interface velocity and the NM EOS, we calculated the stress in the NM. For consistency, only the stress values calculated with the second method are reported in Table I.

The radiance signal was collected directly with a step-index optical fiber with a numerical aperture (NA) of 0.22 and diameter of $910 \mu\text{m}$ (Thorlabs, FG910LEC). The output of the fiber was contact coupled to an array of four smaller ($400 \mu\text{m}$ diameter) step-index fibers. We split one of the four fibers to send the signal to detectors through 50 nm wide band-pass filters centered at 490 and 530 nm . The next fiber in the array was also split, sending the signal to detectors through 50 nm wide band-pass filters at 620 and 690 nm . The third fiber was connected to a four-channel detector system with wavelengths centered at 1140 , 1350 , 1570 , and 1900 nm ; each filter was about 300 nm wide. We used different channels to calculate the temperature in each experiment depending on the radiance spectrum and voltage settings of the oscilloscope.

In some of the experiments documented in this work, the fourth optical fiber was connected to a gated spectrometer. A Princeton Instruments IsoPlane 160 spectrometer was paired with an Andor gated, intensified charge-coupled device (CCD), which we used to measure the time-integrated emission spectrum ($400\text{--}800 \text{ nm}$) of the experiments. We varied the gate width from 0.75 to $2 \mu\text{s}$, depending on the experiment. All the pyrometry channels were calibrated with a blackbody source at a range of temperatures up to 1973 K . The radiance signals were converted to temperature values after being corrected for absorbance in the unshocked NM and motion of the shock and detonation waves during the experiment. The NM absorption spectrum was measured, and we used it to

Effect of a collapsing gas bubble on the shock-to-detonation transition in liquid nitromethane

calculate the absorption depth for each channel. The distance that the radiance traveled through the unshocked NM changed with time during the shot and was determined from the camera images. More detailed commentary on the temperature accuracy of each shot is given in the Appendix. For clarity, only single-temperature traces are shown.

The visible light framing camera captures a series of nine images. We configured the camera with an inter-

frame time of ~ 400 ns and an integration time of ~ 100 ns. An expendable long-pulse, broad-spectrum xenon flashlamp backlit the experiment package for the framing camera. We found it necessary to place an optical diffuser in the form of a plastic holographic diffuser (not shown in Fig. 2) near the package to obtain good-quality images. The diffuser helped minimize the optical artifact of dark regions from refractive index changes in the compressed NM at the leading edge of the shock wave.

TABLE I. Experimental details and continuum parameters.

Experiment	Impactor velocity (km/s)	Package interface velocity (km/s) ^a	Package interface pressure (GPa) ^b	Shock velocity (km/s) ^c	Measured peak temperature (K)	Bubbles (Y/N) ^d	Detonation (Y/N) ^d	Run-to-detonation or bubble-to-detonation time ^e (μ s)
1	2.058	1.63	7.90	4.30	1100	N	N	NA
2	2.248	1.76	8.95	4.51	4000	N	Y	1.91
3	2.096	1.65	8.10	4.34	2700	Y	N	NA
4	2.229	1.75	8.84	4.48	3600	Y	Y	0.54
5 (repeat of 4)	2.265	1.77	9.04	4.52	3600	Y	Y	0.54
6 (repeat of 2)	2.279	1.78	9.12	4.54	3600	N	Y	1.5

^a Package interface velocity is calculated from the measured impactor velocity and the equations of state of the aluminum impactor, PMMA, and NM. Using the (Winey *et al.* 2000) NM EOS, the values are within $\pm 2\%$ of the measured velocity of the package interface when the shock enters the NM. Package interface is where the PMMA and its thin aluminum reflecting cover meet the NM.

^b Pressure determined from measured velocities and NM EOS as described in text.

^c Shock velocity calculated from aluminum impactor velocity (measured with OBI) and NM EOS parameters.

^d *Bubbles* and *Detonation* indicate whether either was present.

^e Run-to-detonation times are measured from the initial shock to the time when the detonation wave overtakes the shock.

III. EXPERIMENTAL RESULTS

We conducted a total of six experiments to compare shocked nondetonating and detonating NM samples with and without a collapsing butane bubble in the stress range between ~ 8 and 9 GPa. This section presents and compares the results of these experiments.

A. Shock wave with no bubble (experiment 1)

In experiment 1, we studied shocked and nondetonating NM with no butane bubble. The initial pressure was 7.9 GPa. The PDV spectrogram is shown in Fig. 3. The data show steady interface and shock wave velocities that remain reflective to the PDV laser light as the shock propagates across the sample. About 1.5μ s after shock enters NM, the shock wave velocity begins to drop slightly due to edge releases, and at 1.8μ s, the signal disappears as the wave approaches the fiber probe. The interface velocity remains steady with a slight step down near 0.9μ s due to wave reverberation in the PMMA buffer and a more substantial drop due to edge releases just before the shock wave comes into contact with the optical probe. The temperature reaches a steady value of 1100 K

at 500 ns after the shock enters the NM and begins to drop slightly when the shock velocity decreases.

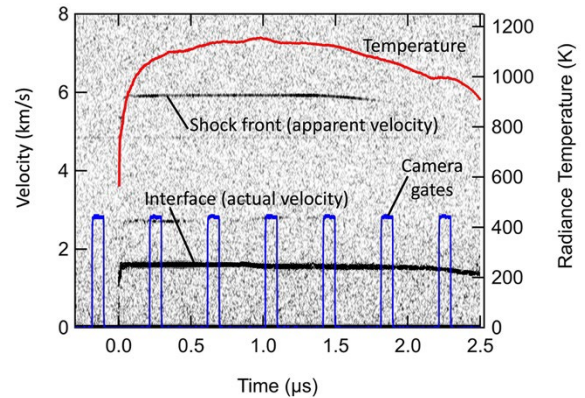


FIG. 3. Apparent velocity spectrogram (black, left axis) and temperature (red, right axis) for experiment 1, where there was no bubble and no detonation. The NM shock wave and package interface surface profiles are the only remarkable features in the velocity spectrogram. The temperature increases to a steady value after the shock enters the NM and then slowly decreases as the shock begins to be overtaken by edge releases at $\sim 1.5 \mu$ s. The electrical fiducials (blue) associated with the first seven camera frames (1–7) are also shown.

Effect of a collapsing gas bubble on the shock-to-detonation transition in liquid nitromethane

Images (frames 2–7) from experiment 1 are shown in Fig. 4. The time of each frame relative to shock arrival in the NM sample is noted. The shock propagates from left to right in the sequence of images. The shock front develops some curvature as edge release waves begin to enter the experiment. The opacity of the leading edge of the shock wave in the later frames is likely due to lensing from the curved surface of the shock wave.

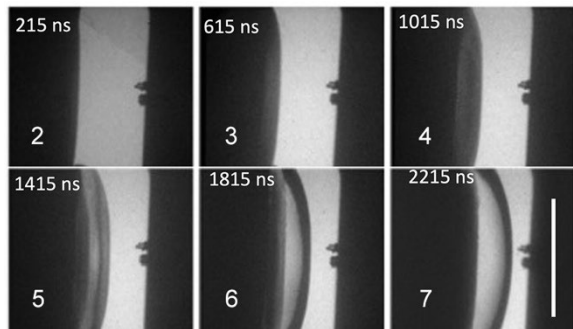


FIG. 4. Time sequence (frames 2–7) of images for experiment 1, showing shocked NM with no detonation and no butane bubble. The shock enters from the left and propagates to the right (in each row of frames). In each frame, the time after the shock enters the NM is noted at the top left-hand corner and frame number at the bottom left-hand corner. Artifacts at right center of the NM are instrumental. The length scale is given by the 11 mm long white bar at the right in frame 7.

B. Detonation with no bubble (experiment 2 and repeated in experiment 6)

Figure 5 shows the results of experiment 2. No butane bubble was introduced in this experiment. Its faster impactor gave a higher initial pressure than experiment 1, which resulted in a detonation. The calculated initial stress was 8.9 GPa. The velocity spectrogram for experiment 2 shows several distinct features. At early times, the interface velocity and shock wave velocity are steady, as in the nondetonating case; however, the interface velocity signal disappears at about 1.2 μs after the shock enters the NM. Then at 1.9 μs , the apparent velocity rises sharply to a peak of about 10 km/s (actual velocity of 7.3 km/s), followed by a decaying shock front. We believe this to be an overdriven detonation (Chaiken 1960) that decays within 200 ns to a steady detonation wave. This overdriven signal was observed only when we used the two-fiber PDV optical probes. The steady detonation wave has little reflectance of the PDV laser light, and prior observations by Mercier *et al.* (2010) reported zero reflectivity using embedded PDV optical fibers. The detonation wave does not appear as a steady single velocity but instead shows a spread in apparent velocities (darker region after 2.1 μs in Fig 5) ranging from 7.8 to 9.5 km/s (actual velocity range 5.7 to 6.9 km/s).

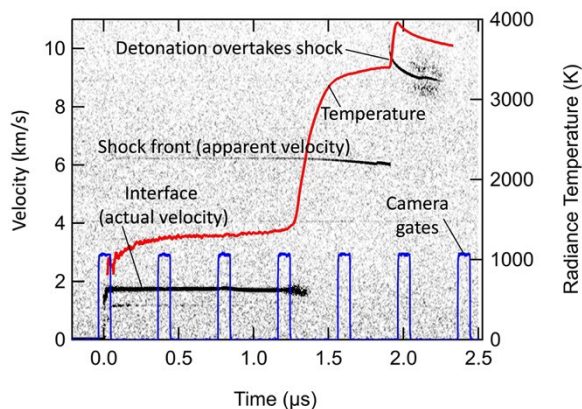


FIG. 5. Apparent velocity spectrogram (black, left axis) and temperature (red, right axis) for experiment 2, where the NM detonates without a butane bubble. Several interesting features are noted in the velocity spectrogram, including a broad velocity spectrum after 2.0 μs from a reflection off the steady detonation front. The electrical fiducials (blue) associated with the first seven camera frames (1–7) are also shown.

As in experiment 1, the temperature rises to a relatively steady value of 1300 K until about 1.2 μs after the shock enters the NM. When a detonation wave forms in the volume behind the shock front, the temperature rises sharply to an asymptotic value of 3400 K. The onset of this temperature rise is coincident with the loss of the velocity signal from the package interface. The temperature jumps sharply again, peaking at 3960 K, when the detonation front overtakes the shock front at 2.0 μs . Subsequently, the temperature decays (along with the velocity) to a value of ~ 3700 K. The temperature trace shown in Fig. 5 is stitched together from several pyrometry channels. The 1900 nm channel was used to measure temperatures from 800 to 2500 K; this channel saturated at temperatures >2500 K. We used four other channels (530–1350 nm) to measure temperatures in the ~ 1500 –4000 K range. Differences in temperature measurements from these pyrometry channels were within ± 50 K.

Figure 6 shows framing camera images (frames 2–7) captured in experiment 2. A detonation event appears to form about 1.3 μs after the shock enters NM. This phenomenon is not indicated as a distinct wave but appears as a volumetric feature emanating from a point source within the portion of the shocked NM. The detonation initiates near the center of the impact, where edge effects are the smallest and the peak stress lasts the longest. The detonation begins between frames 4 and 5 and is coincident with an asymptotic rise in the temperature and a loss of the PDV signal from the package interface. In frame 5, an isotropic, radiating feature forms behind the shock front and begins to propagate within the shocked NM. This feature has a velocity of ~ 6 km/s, consistent with a detonation wave. Frame 6 shows this feature overtaking the shock front and entering the unshocked NM. This timing is coincident with sharp increases in the velocity of the wave front and the temperature.

Effect of a collapsing gas bubble on the shock-to-detonation transition in liquid nitromethane

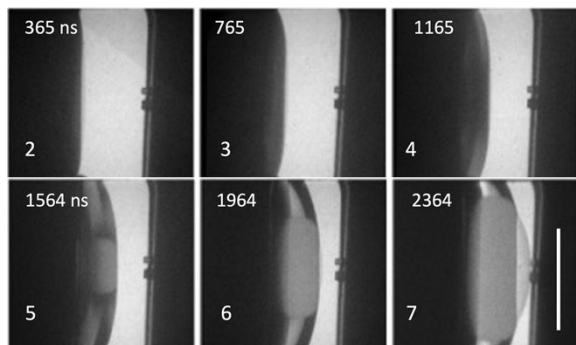


FIG. 6. Time sequence of images (frames 2–7) for experiment 2, showing shocked and detonating NM with no butane bubble. The shock enters from the left and propagates to the right (in each row of frames). In each frame, the time after the shock enters the NM is noted at the top left-hand corner and frame number at the bottom left-hand corner. Artifacts at right center of the NM are instrumental. The length scale is given by the 11 mm long white bar at the right in frame 7.

C. Bubble collapse experiment without detonation (experiment 3)

Figure 7 shows results of experiment 3, which had a butane bubble collapse but no sustained detonation. The initial pressure was 8.1 GPa. The package interface velocity profile is visible for the first $\sim 0.7 \mu\text{s}$ and then drops out when the shock wave collapses the bubble. The shock wave was not resolved with the collimated PDV probes used in this experiment. Consequently, the initial NM pressure of 8.1 GPa was calculated from the impactor velocity. Also, for this experiment, the radiance recording system sensitivity was set too low to record a signal before the shock reaches the bubble. After the bubble collapse, the temperature rises to a peak value of 2700 K, lower than that observed during a full detonation (experiment 2), and then slowly decays. The radiance appears to come primarily from the dark material that forms after the bubble collapse.

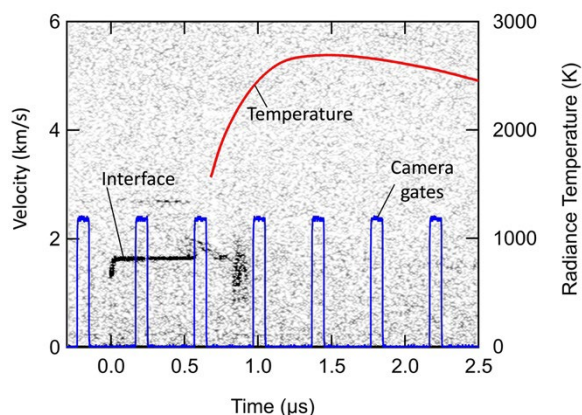


FIG. 7. Velocity spectrogram (left axis, black) and temperature (right axis, red) for experiment 3, where there was a collapsing butane bubble but no detonation. The drive surface profile is visible for the first $\sim 0.7 \mu\text{s}$ and then disappears simultaneously with the bubble collapse. The temperature shows a distinct rise when the bubble is overtaken by the shock wave and collapses (at 567 ns, as shown in frame 3 in Fig. 8). The electrical fiducials (blue) associated with the first seven camera frames (1–7) are also shown.

Images (frames 2–7) from experiment 3 are shown in Fig. 8. To measure the transparency of the shocked NM qualitatively, we placed a transparent plastic grid between the flashlamp and the input window to the experiment package. Before the shock arrives (167 ns, frame 2), the grid is visible throughout the optical view, and the bubble appears as a dark, roughly oblique object (likely a flattened sphere in 3D), vertically centered and near the left side of the NM cell. The shock front appears first in frame 2 and overtakes the bubble by frame 3. By frame 4, the bubble has collapsed.

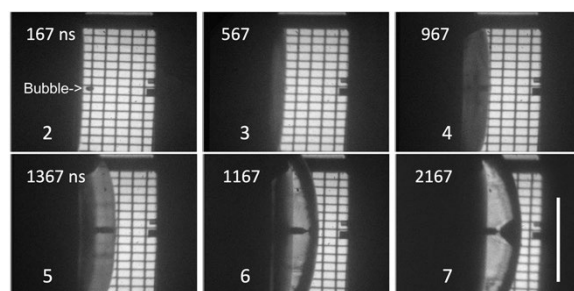


FIG. 8. Time sequence of images (frames 2–7) for experiment 3, showing shocked and nondetonating NM with a butane bubble. The shock enters from the left and propagates to the right (in each row of frames). In each frame, the time after the shock enters the NM is noted at the top left-hand corner and frame number at the bottom left-hand corner. A grid placed behind the experiment shows transmission through the shocked NM. Artifacts at right center of the NM are instrumental. The length scale is given by the 11 mm long white bar at the right in frame 7.

Unlike the collapse of helium gas bubbles in prior studies (Turley *et al.* 2021), the butane bubble collapse does not result in a large local flash of light. Given the higher molecular weight and lower ratio of specific heats, C_P/C_V , of butane, the temperature rise caused by shock collapse of a bubble is much lower in butane than in helium. The butane

bubble collapse shown in frame 3 is coincident with a rise in the temperature and a sudden drop in the PDV signal from the package interface. A zone of opacity forms where the bubble collapses. This may be associated with the onset of reactive growth but does not lead to sustained detonation. Frame 5 shows that a local opaque zone forms near the bubble collapse region. Also, an isotropic wave is launched radially behind the shock front and propagates at a velocity on the order of 4.6 km/s, indicative of a shock wave in compressed NM, probably a result of the bubble collapse. Between frames 6 and 8 (not shown in Fig. 8), the opaque region grows to a size on the order of ~ 3 to 4 mm in diameter. During this time frame, the temperature peaks and then drops. Although the curvature of the shock wave in the later images probably causes lensing and distortion, the grid is still visible behind this wave, suggesting that the NM remains transparent outside of the opaque region.

As discussed in Bourne and Field (1991, 1999), Bourne and Milne (2002, 2003), and Michael and Nikiforakis (2019a), when the shock front reaches a cavity, a jet of NM likely forms inside the bubble where it is first shocked. The jet propagates at high speed and impacts the opposite wall of the cavity. At the point of collision, the jet generates a high-pressure shock with the highest NM temperature anywhere in the bubble collapse process. The collision of the NM jet and bubble wall is believed to initiate a precursor chemical reaction and the formation of the opaque region resulting from NM reaction products. Also, the collapsed bubble is likely the source of the wave propagating radially out from this region. As discussed in detail in Michael and Nikiforakis (2019a), there are likely other shocks formed during the bubble collapse process in addition to the jet collision, but in our images, they are not resolved and seem to coalesce into a single shock at later times. The shape of the opaque region is similar to shapes predicted in spherical cavity collapse simulations by Michael and Nikiforakis (2019a).

D. Bubble collapse experiment with detonation (experiment 4 and repeated in experiment 5)

In experiment 4, a single butane bubble was introduced. The combination of shock impact and bubble collapse led to detonation. Velocimetry and temperature data for this experiment are shown in Fig. 9. The initial pressure was 8.8 GPa. As in experiments 1, 2, and 3, the temperature for the first 0.5 μs after the initial shock is relatively steady at a value of 1260 K. The rise in temperature from this steady value begins immediately upon bubble collapse at ~ 600 ns after the shock enters NM at the package interface. Unlike experiment 2, in which we observed a two-step temperature increase process, experiment 4 results in a monotonic temperature increase to a peak of 3630 K before the temperature drops asymptotically to 3420 K. Also, the interface velocity continues to be resolved during the temperature rise, with the signal dropping out after the peak temperature is reached. The run-to-detonation time is much shorter than in

experiment 2 (Fig. 5), indicating that the bubble sensitized the NM.

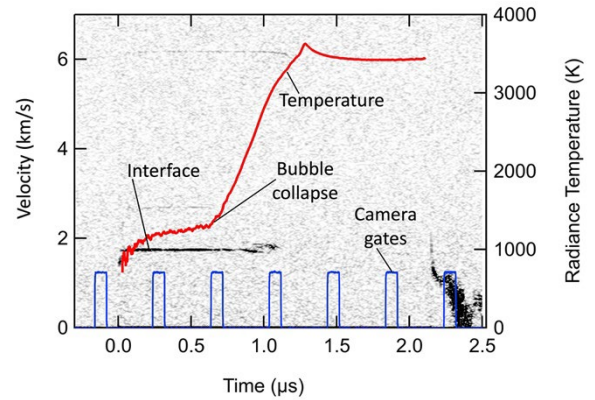


FIG. 9. Velocity spectrogram (black, left axis) and temperature (red, right axis) for experiment 4, where there was a single collapsing butane bubble followed by NM detonation. The package interface velocity profile and shock wave are visible for the first ~ 1 μs and then disappear after the bubble collapse and rise in temperature. The detonation wave was not resolved with the collimated PDV probes used here. The electrical fiducials (blue) associated with the first seven camera frames (1–7) are also shown.

Figure 10 shows framing camera images (frames 2–7) from experiment 4. The bubble collapse in frame 4 was carefully timed so it would occur in the field of view of the radiance optical fiber in the center of the package. These images show an optical feature indicating that the NM detonation is initiated at the time and location of the bubble collapse. When the bubble collapses, this feature radiates within the shocked and unshocked NM. Using the calibrated images, we estimated the speed of its leading edge in the shocked NM to be 6.1 km/s, consistent with the measured shock velocities measured with PDV in experiments 1, 2, and 4. The temperature trace shown in Fig. 9 is stitched together from several pyrometry channels. Four channels, with wavelengths from 1140 to 1900 nm, were used to measure temperatures from 800 to 2500 K before the temperature began to ramp up near 0.7 μs . These channels saturated around 2500 K. Four other channels (530–1350 nm) were used to monitor temperatures in the range of 1500 to 4000 K.

Effect of a collapsing gas bubble on the shock-to-detonation transition in liquid nitromethane

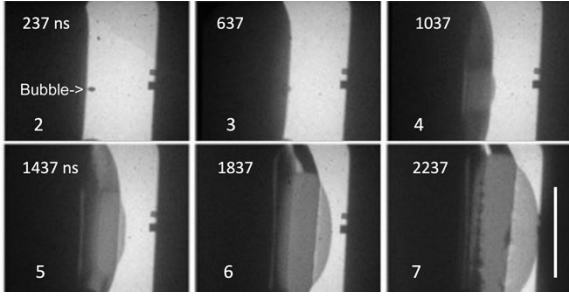


FIG. 10. Time sequence of images for experiment 4, showing NM detonation with a single butane bubble. The initiation of the detonation is clearly associated with the location of the bubble collapse in frame 4 (1037 ns). The shock enters from the left and propagates to the right (in each row of frames). In each frame, the time after the shock enters the NM is noted at the top left-hand corner and frame number at the bottom left-hand corner. Artifacts at right center of the NM are instrumental. The length scale is given by the 11 mm long white bar at the right in frame 7.

For comparison, all the temperature profiles from experiments 1 to 4 are plotted together in Fig. 11.

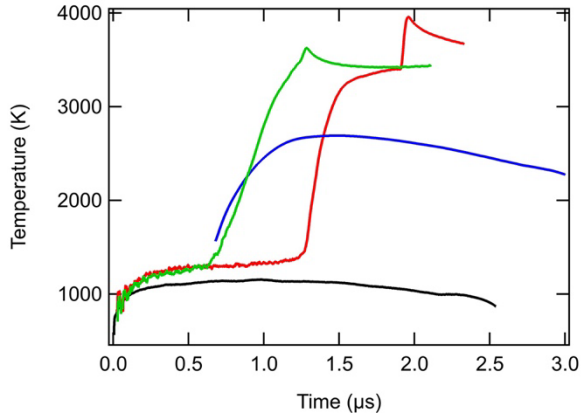


FIG. 11. Temperature profiles for experiments 1 (black), 2 (red), 3 (blue), and 4 (green).

IV. MODELING AND SIMULATION

Recently, an improved reactive flow model was developed for HE burn by Aslam (2018). We used this model with a thermodynamically complete EOS and a reactive flow model of NM to simulate the results of the experiments described in Sec. III. The empirical Davis reactant and the product EOS are both based on experimental data, as well as higher-fidelity models from molecular dynamics simulations and thermochemical codes. Although the Arrhenius-Wescott-Stewart-Davis (AWS) reactive flow model (Aslam 2018) was originally developed for heterogeneous PBX, it can capture the salient features of homogeneous shock initiation, including superdetonation prior to turnover, observed experimentally in shock-to-detonation transition experiments. This property occurs because the model rate form has Arrhenius sensitivity to local temperature with a suitable choice of parameters. We used the temperature and velocity data from the experimental datasets to

calibrate the AWS rate parameters. Full details of the model calibration are presented in Aslam *et al.* (2024).

The simulations utilized a grid spacing of $6.25 \mu\text{m}$ and covered a domain of $0 \text{ mm} < r < 18 \text{ mm}$ and $-9 \text{ mm} < z < 12.7 \text{ mm}$, where $r = 0$ is the axis of symmetry and $z = 0$ is the boundary of the PMMA and NM. The computations started at a time $t < 0$ such that the shock entered NM at $z = 0$ and at $t = 0$.

In these experiments, the finite radius of the aluminum impactor causes lateral release waves to enter the domain. We modeled the air surrounding the aluminum impactor as NM products with an initial pressure of 0.1 MPa (roughly 1 atm of pressure) and density of 0.2 mg/cm^3 .

Because experiments 1 and 2 have no butane bubble, we can model simulations assuming 2D and axial symmetry. Experiments 3 and 4 have a bubble that is not perfectly spherical, and in reality, it is flattened. To model this geometry precisely would require a full 3D simulation, which is beyond the scope of the present investigation. Rather, as a rough approximation, we modeled the bubble as spherical to examine the effects of bubble collapse during the shock initiation of NM. In experiments 3 and 4, the butane bubble was modeled simply as NM products with a density of 2.5 mg/cm^3 . To roughly match the total volume of butane as observed in the experiments, we set the bubble radius to 0.58 mm, and the center of the bubble was located 2 mm from the PMMA-NM interface.

To compare to experimental observations, we integrated a tracer particle located initially at $r = 0$ and $z = 0$ with the computed fluid velocity, and we recorded its axial particle velocity as a function of time. Additionally, we estimated the shock arrival time, $t_a(r, z)$, at all computational cells by computing the first time a computational cell density went above 1.4 g/cm^3 . We computed the shock velocity, s , by using the Eikonal equation, $s = 1/|\text{grad}(t_a)|$. This must be computed carefully, as numerical errors can lead to $O(1)$ errors. We followed the procedure outlined in Aslam, Bdzil, and Hill (1998).

To compare to the experimental temperature measurements, we computed T_{max} , which corresponds to the maximum temperature seen along the entire axis of symmetry as a function of time. In some sense, T_{max} is the maximum temperature one would expect to see when comparing to experiments.

A. Model simulation of experiment 1

The simulated PMMA-NM interface velocity, shock velocity, and temperature (T_{max}) for experiment 1 are shown in Fig. 12(a). The model simulation jumps off at 1.619 km/s, which is very close to the measured velocity of 1.63 km/s) given in Table I. The corresponding shock temperature is initially computed to be roughly 880 K. The simulated temperature rises by $\sim 100 \text{ K}$ between $t = 0$ and $1.5 \mu\text{s}$ due to a small amount of reaction. At $1.5 \mu\text{s}$, release waves reach the centerline and begin to lower both the simulated velocity and temperature, indicating that the simulation will not reach detonation. Data extracted from Fig. 3 are shown in Fig. 12(b). It shows that the model agrees well with the

Effect of a collapsing gas bubble on the shock-to-detonation transition in liquid nitromethane

measured velocities, but the computed temperature is too low.

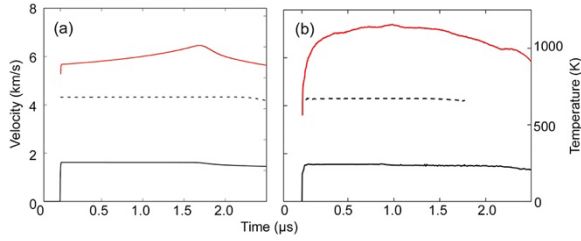


FIG. 12. Experiment 1. (a) Model-computed PMMA-NM interface velocity (solid black), shock velocity (dashed black), and temperature T_{max} (red) vs time. (b) Measured interface velocity (solid black), shock velocity (dashed black), and radiance temperature T_{max} (red) vs time. Because the emissivity is not known, only the radiance temperature is measured. Radiance temperature assumes $\epsilon = 1$, so it is a lower limit to the actual temperature.

Figure 13 shows the simulated density fields at various times. It shows how the lateral release waves reach the centerline, and in this case, detonation is not achieved.

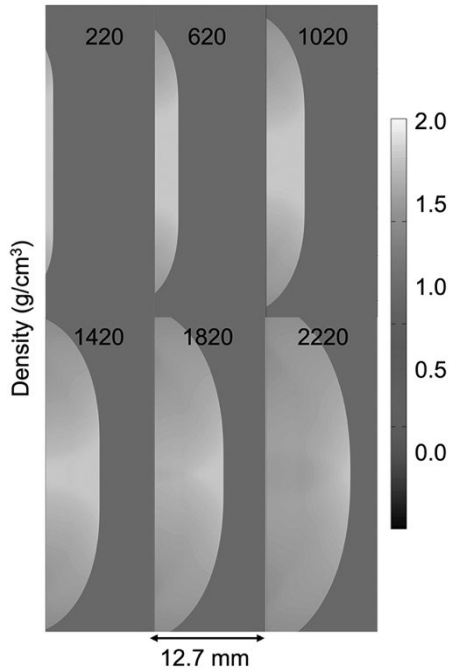


FIG. 13. Simulated density fields at roughly the same times as shown in Figs. 4 and 12 for experiment 1. Frames are labeled with simulation times in ns. The scale at the right shows the density in g/cm^3 .

B. Model simulation of experiment 2

The simulated PMMA-NM interface velocity, shock velocity, and temperature (T_{max}) for experiment 2 are shown in Fig. 14(a). The model simulation jumps off at 1.752 km/s, which is very close to the measured velocity (1.76 km/s) given in Table I. The corresponding shock temperature is initially computed to be roughly 970 K. The simulated maximum temperature along the centerline rises slowly at first and then seems to run away

just before 1 μs , resulting in a superdetonation. As the superdetonation reaches fresh material and transits to an overdriven detonation at 1.5 μs , the maximum temperature jumps and then slowly decays as the overdriven detonation decays toward the Chapman-Jouguet condition; this is seen in Fig. 14(a) from examination of the resulting shock velocity. The glitch in T_{max} near $t = 2.4 \mu\text{s}$ is due to the leading shock reaching the edge of the computational domain. In the measurements, the temperature is consistent with the modeled temperature if the emissivity is assumed to be ~ 0.7 . The velocities are also in agreement, but the times of the artifacts are different.

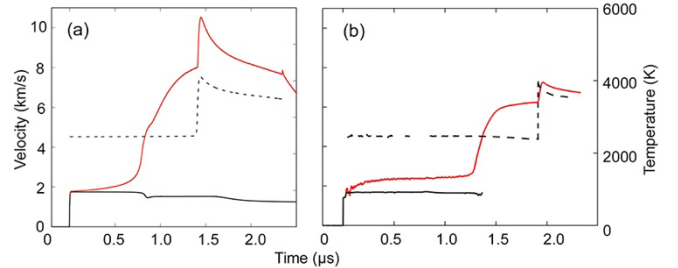


FIG. 14. Experiment 2. (a) Model-computed PMMA-NM interface velocity (solid black), shock velocity (dashed black), and temperature T_{max} (red) vs time. (b) Measured interface velocity (solid black), shock velocity (dashed black), and radiance temperature T_{max} (red) vs time. Because the emissivity is not known, only the radiance temperature is measured. Radiance temperature assumes $\epsilon = 1$, so it is a lower limit to the actual temperature.

Figure 15 shows the simulated density fields at various times.

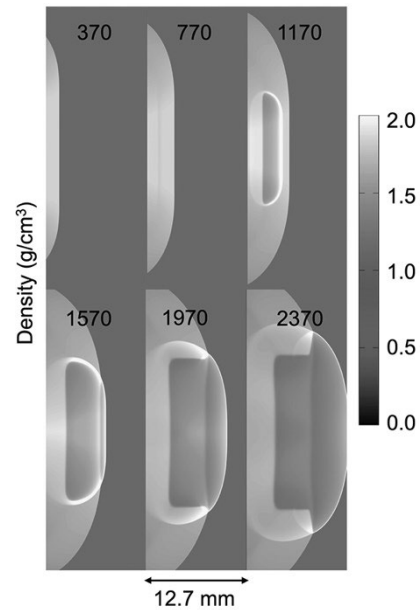


FIG. 15. Simulated density fields at roughly the same times as shown in Figs. 6 and 14 for experiment 2. Frames are labeled with simulation times in ns. The scale at the right shows the density in g/cm^3 .

C. Model simulation of experiment 3

The simulated PMMA-NM interface velocity, shock velocity, and temperature (T_{max}) for experiment 3 are shown in Fig. 16(a). The model simulation jumps off at 1.646 km/s, which is very close to the measured velocity (1.65 km/s) given in Table I. The corresponding shock temperature is initially computed to be roughly 905 K. The simulated maximum temperature along the centerline rises very slowly at first and becomes quite high in the shocked bubble upon collapse near 0.6 μ s. Generally, the observed T_{max} is in the range of 3000 to 4000 K after the bubble collapse, whereas the experiment appears to be in the range of 2000 to 3000 K. The computed shock velocity is somewhat meaningless between 0.3 and 0.6 μ s when the shocked NM is overtaking the bubble. Also, in this time frame, the computed temperature profile may be dominated by the gas temperature rise that occurs when the bubble collapses. There is not a large shock velocity increase after 1 μ s.

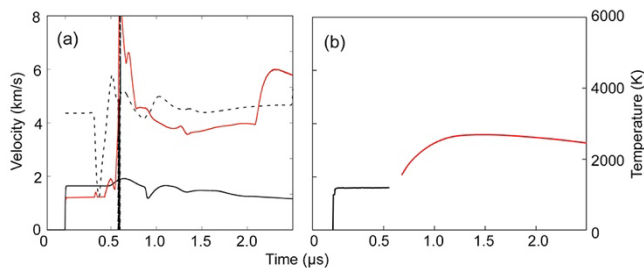


FIG. 16. Experiment 3. (a) Model-computed PMMA-NM interface velocity (solid black), shock velocity (dashed black), and temperature T_{max} (red) vs time. The vertical feature near 0.6 μ s is from oscillations in the computation when the shock overtakes the bubble. (b) Measured interface velocity (solid black) and radiance temperature T_{max} (red) vs time. The shock velocity measurement failed on this experiment. Because the emissivity is not known, only the radiance temperature is measured. Radiance temperature assumes $\epsilon = 1$, so it is a lower limit to the actual temperature.

Figure 17 shows the simulated density fields at various times, where we see a chevron shape due to reactivity in material near the bubble and along a Mach stem region off-center. Figure 8 shows a somewhat similar triangular region near the centerline at 2167 ns (frame 7). At a later time (near 2.6 μ s), the model predicts a transition to detonation at the centerline.

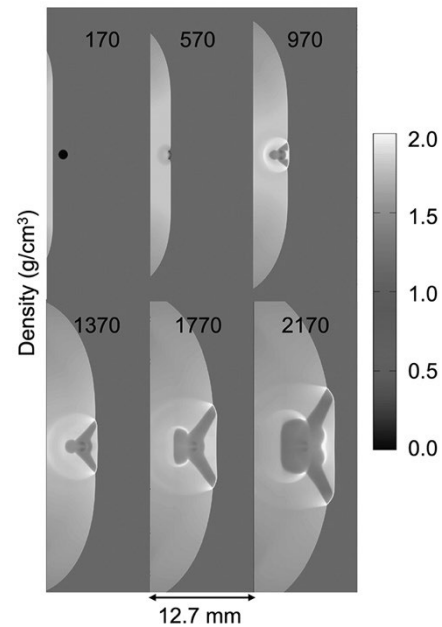


FIG. 17. Simulated density fields at roughly the same times as shown in Fig. 8 for experiment 3. Frames are labeled with simulation times in ns. The scale at the right shows the density in g/cm^3 .

D. Model simulation of experiment 4

The simulated PMMA-NM interface velocity, shock velocity, and temperature (T_{max}) for experiment 4 are shown in Fig. 18(a). The model simulation jumps off at 1.739 km/s, which is very close to the measured velocity (1.75 km/s) given in Table I. The corresponding shock temperature is initially computed to be roughly 965 K. After the bubble collapses, there is a spike in the simulated maximum temperature along the centerline, and it stays in the 3000–5000 K range. After the bubble collapse, the computed shock velocity oscillates slightly but is clearly increasing toward the Chapman-Jouguet detonation velocity (D_C).

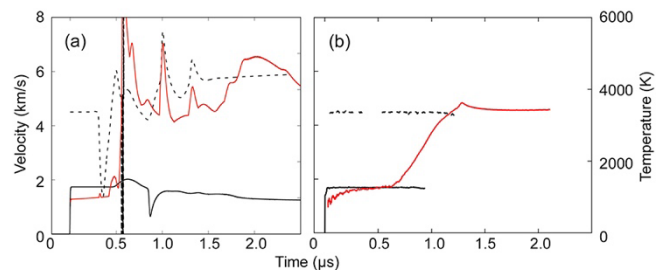


FIG. 18. Experiment 4. (a) Model-computed PMMA-NM interface velocity (solid black), shock velocity (dashed black), and temperature T_{max} (red) vs time. The vertical feature near 0.6 μ s is from oscillations in the computation when the shock overtakes the bubble. (b) Measured PMMA-NM interface velocity (solid black), shock velocity (dashed black), and radiance temperature T_{max} (red) vs time. Because the emissivity is not known, only the radiance temperature is measured. Radiance temperature assumes $\epsilon = 1$, so it is a lower limit to the actual temperature.

Figure 19 shows the simulated density fields at various times where, after the bubble collapse, we observe

reactivity (shown as lower density) near the bubble, as well as at larger radii. The model likely would indicate detonation even if there were not a bubble present.

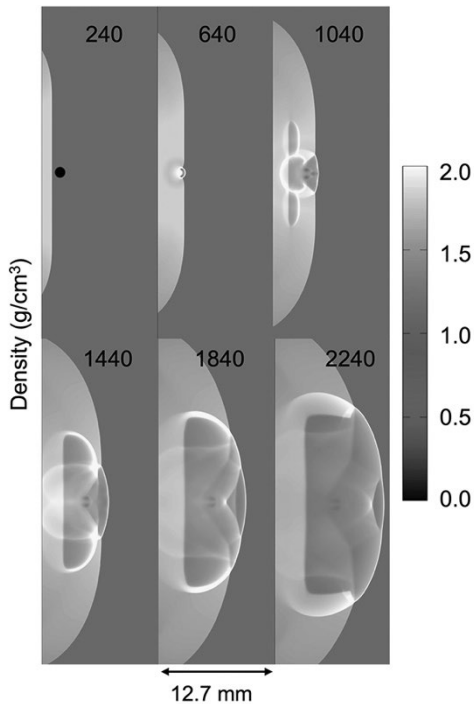


FIG. 19. Simulated density fields at roughly the same times as shown in Fig. 10 for experiment 4. Frames are labeled with simulation times in ns. The scale at the right shows the density in g/cm^3 .

V. CONCLUSION

We conducted a series of shock wave experiments on liquid explosive NM loaded with a single bubble of butane to investigate the role of void collapse and subsequent hot spot formation in the detonation process. Simulations have been done on bubble collapse in NM and published by Bourne and Field (1991, 1999), Bourne and Milne (2002, 2003), and Michael and Nikiforakis (2019a), but there has been relatively little experimental work diagnosing the bubble and its effects on the processes associated with the onset of detonation. Our experiments were diagnosed with optical imaging, velocimetry, time-resolved pyrometry, and time-integrated spectroscopy. Experiments to study shocked NM in the absence of bubbles were also performed for comparison. The shock velocity and radiance temperature data presented in this work agree with those in prior studies done on undetonated NM. In the bubble experiments, the bubble collapse either initiated the incipient chemical reactions or led to sustained detonation of the NM or both. Our results are in good agreement with the three-part bubble implosion process proposed by Bourne and Milne (2002, 2003).

In the visible imaging, clear evidence of the detonation process occurs near the bubble collapse, showing the multi-wave structure of shocked and detonating material.

When the shock wave overtakes the bubble, a new wave forms at the bubble collapse location, propagates into the shocked NM, and eventually overtakes the shock wave. The velocity of this wave was consistent with either shock propagation or steady detonation, 4.6 or 6.1 km/s, respectively, depending on the experiment.

For all experiments, the spectrometer data show broad, structureless emission that can be fit to a Planck function to estimate temperature. The optical pyrometry measurements of shocked and undetonated NM are consistent with previous measurements and simulations (Turley *et al.* 2021) for the pressure ranges of our study. In those cases where detonation occurs, the pyrometry signal is consistent with the stepwise detonation model of Chaiken (1960), starting with a region of reactive flow, followed by superdetonation and overdriven detonation, and eventually steady detonation. With a bubble and no detonation, the opaque region near the bubble collapse is consistent with chemical reactions having taken place near the bubble. The overall structure of the opaque region is in qualitative agreement with simulations performed by other authors on spherical voids (Bourne and Field 1991, 1999; Bourne and Milne 2002, 2003; and Michael and Nikiforakis 2019a). It should be noted that the scope of our work ignores any possible chemical reactions between the NM and the butane released upon bubble collapse, even though this may have contributed to the detonation.

Velocimetry measured with PDV was invaluable to these experiments; both the shock and interface velocities were measured. In experiments in which detonation took place, the reflections from the PMMA surface disappeared during detonation onset, indicating that the detonation wave front became opaque and absorbed the PDV light. In most of the experiments with detonations, we also observed partial reflections of the PDV light from the detonation wave. Rather than a single velocity value for reflective shocks in non-reacting NM, there was a large spread in velocities centered on the nominal detonation speed for the detonating wave. This suggests a complex structure at the front of the detonation wave. In one experiment, experiment 2, we observed a decaying overdriven detonation wave just before steady detonation began.

One difference between this experimental work and prior simulations of bubble collapse is that earlier simulations assumed spherical bubbles, whereas we had large, flattened bubbles. This difference adds a complexity to the simulations and makes it more difficult to quantify the experimental results. Nevertheless, the spherical simulations, particularly in Bourne and Field (1991, 1999), Bourne and Milne (2002, 2003), and Michael and Nikiforakis (2019a), were instrumental in helping us understand what was happening in the experiments, and our results appear to verify their descriptions of the bubble collapse process.

We also performed simulations assuming a spherical bubble with a volume comparable to the experimental bubbles. We saw several interesting aspects when comparing these simulations to the experimental data.

Very generally speaking, we observed several aspects in the simulations that exist in the experimental measurements, including increased detonation sensitivity when including voids/bubbles in homogeneous liquid explosives such as NM. We also made two important observations when making detailed comparisons here. First, the model seems to transition to detonation slightly earlier than the experiments. As pointed out in Aslam *et al.* (2024), the data utilized to calibrate the model ignore the embedded computational gauge package (modeled in 1D). It is likely that the gauge package in the computations leads to reflected waves that increase the pressure and temperature and cause a slightly earlier reaction than might be the case if the gauge package were not there. Our experiments utilized optical instrumentation that perturbs the flow less than in the model, although detailed flow information was not collected during the experiments. Second, it is clear that once detonation does occur, the simulated temperatures are often 1000 to 2000 K higher than measured values. As we have seen in other AWS models, this is likely because the Davis-products EOS is problematic at high temperatures, as it is assumed to have a constant specific heat. Detailed thermochemical codes, such as obtained with Magpie (Ticknor *et al.* 2020) and density functional theory calculations (Leiding *et al.* 2024), show that the specific heat changes by roughly a factor of 3 as the temperature rises from 1000 to 8000 K. Similar changes are observed for the Grüneisen parameter along an isochor over that same temperature range. Utilizing a non-Mie-Grüneisen EOS, such as Lozano *et al.* (2023), may lead to a significantly better modeling paradigm.

ACKNOWLEDGMENTS

The authors are grateful for the invaluable technical support from Ruben Valencia (Nevada National Security Sites, Special Technologies Laboratory) in the fabrication and assembly of the experimental packages and assisting with execution of the dynamic experiments.

This manuscript has been authored by Mission Support and Test Services, LLC, under Contract No. DE-NA0003624 with the U.S. Department of Energy, the National Nuclear Security Administration's Office of Defense Programs, and supported by the Site-Directed Research and Development Program. Portions of this work were supported by Triad National Security, LLC, under Contract No. 89233218CNA000001 with the U.S. Department of Energy, National Nuclear Security Administration. The United States Government retains and the publisher, by accepting the article for publication, acknowledges that the United States Government retains a non-exclusive, paid-up, irrevocable, worldwide license to publish or reproduce the published form of this manuscript, or allow others to do so, for United States Government purposes. The U.S. Department of Energy will provide public access to these results of federally sponsored research in accordance with the DOE Public Access Plan (<http://energy.gov/downloads/doe-public>

-access-plan). The views expressed in the article do not necessarily represent the views of the U.S. Department of Energy or the United States Government (DOE/NV/03624--2080).

AUTHOR DECLARATIONS

Conflict of Interest

The authors have no conflicts to disclose.

Author Contributions

W. D. Turley: Conceptualization (equal); Experiment execution (equal); Data analysis (equal); Writing (equal). **B. M. La Lone:** Conceptualization (equal); Experiment execution (equal); Data analysis, Writing (equal). **G. D. Stevens:** Conceptualization (equal); Experiment execution (equal); Data analysis (equal); Writing (equal). **J. G. Mance:** Experiment execution (equal); Data analysis (equal); Writing (equal). **M. D. Staska:** Experiment design and execution (equal). **L. R. Veaser:** Writing (equal); Editing (lead). **T. M. Aslam:** Modeling (lead); Writing (equal). **D. M. Dattelbaum:** Conceptualization (equal); Editing (equal)

DATA AVAILABILITY

The data that support the findings of this study are available within the article. Any other details of interest can be obtained from the corresponding author upon reasonable request.

APPENDIX Determination of temperature uncertainties

The radiance emitted in these experiments must pass through a length of unshocked NM before entering the collection fiber. To determine the actual radiance emitted from the shocked or detonating NM, we need to correct the radiance for the wavelength-dependent absorption, which decreases during the experiment as the shock front moves closer to the collection fiber and the path through unshocked NM gets shorter. From the camera images, we determined the distance vs. time between the fiber and emitting shock front. We then calculated the spectral response for each pyrometer channel using the vendor-supplied spectral responses of the fibers, dichroic splitters, bandpass filters, and photodetectors. Absorption in the visible was negligible but significant in the near IR. The net calculated response for the IR channels, along with the measured extinction coefficient in NM, is shown in Fig. 20.

Effect of a collapsing gas bubble on the shock-to-detonation transition in liquid nitromethane

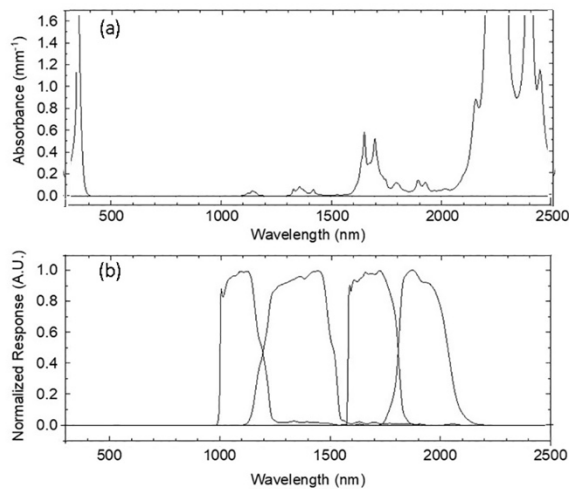


FIG. 20. (a) Ambient pressure NM spectral extinction coefficient. (b) Normalized system spectral response for the four IR pyrometry channels centered at 1140, 1350, 1570, and 1900 nm.

By convolving the calculated system response from each channel with the measured NM absorption spectrum, we calculated the net absorption vs. optical path length for each channel and used this to convert the measured radiance to the actual radiance emitted from the shocked or detonating NM. Figure 21 shows an example (experiment 5) of the radiance temperature measurements before and after corrections are applied assuming emissivity $\epsilon = 1$.

The different channels show radiance temperatures that are closer to agreement after these corrections are applied. The differences in radiance temperature that remain after correction may be due to small differences in emissivity at each wavelength (which may change with time) or other factors. Since radiance temperature is calculated assuming an emissivity of 1, the highest value among all channels gives a lower bound for the temperature.

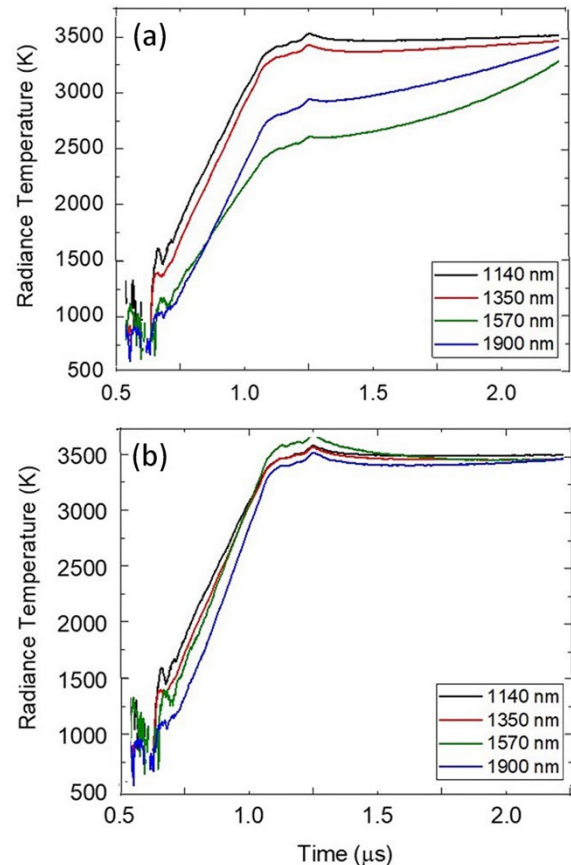


FIG. 21. Example from experiment 5. (a) Radiance temperature measured at several wavelengths. (b) The same measurements corrected for absorption in the unshocked NM.

The experiments outlined in this work measure radiance from either a shocked (but not detonating) volume or plane of NM, a detonating plane of NM, or light emanating from the zone of reacting material that forms after the bubble collapses. Inferring physical temperature from radiance for the shocked NM volume and the bubble reaction zone is difficult. However, for the cases where the NM detonated, our spectral data suggest that the emissivity may be near 1 and that the energy is likely radiating from a high emissivity plane at the detonation front, indicating that the radiance temperature is close to the physical temperature of the detonating NM. To estimate the emissivity of the detonating NM, we fit the radiance spectrum to a gray-body Planck function where the temperature and emissivity were floating fit parameters. The resulting best-fit curves from experiments 2 and 5 are shown in Fig. 22. Both these fits cover the average radiance value for about a microsecond when the temperature was somewhat constant, i.e., the time interval between 1.7 and 2.5 μs in Fig. 21. In both experiments 2 and 5, the emissivity fits a value near 1, indicating the detonation is not transparent. This conclusion is further supported by the PDV data and camera images, which show no transmission through the detonating NM. For a spectrally flat emissivity, the shape of the gray-body curve is determined by the temperature. Because the data we measured fit well with the gray-body

curve, this suggests the radiance temperature is close to the physical temperature for detonating NM. However, it is technically possible to generate emissivity curves that would give equally good fits for any temperature above the value shown in the fits. To estimate a qualitative temperature error, we generated a series of linearly varying emissivity curves ranging from 0.4 to 1, applied them to the data, and used nonlinear fitting to calculate temperature. This gave temperatures ranging from 3445 up to 3750 K, so we assess this range is a reasonable estimate for the physical temperature of the detonating NM.

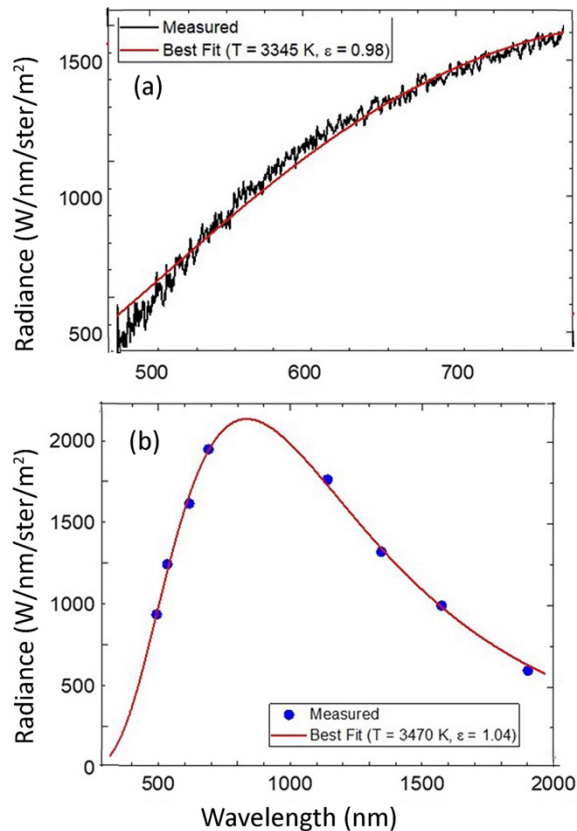


FIG. 22. Radiance spectrum of detonating NM, along with the results of nonlinear fits to a Planck function: (a) spectrum from the intensified CCD spectrometer for experiment 2; (b) spectrum from the photodiodes for experiment 5. The fits support the assumption that the emissivity of detonating NM is close to 1.

We were not able to estimate emissivity using a spectral fit for shocked (nondetonating) NM because the temperature was too low for us to obtain signals from the intensified CCD system, and only the 1900 nm channel had enough radiance for detection. The only inference we can make from the nondetonating NM data is that the radiance temperature reported here places a lower bound on the physical temperature (since emissivity cannot be greater than 1). Furthermore, the shocked NM starts out as a very thin layer, which is likely transparent, then grows and becomes more absorptive as it becomes thicker. Thus, emissivity is likely to increase with time, causing the radiance temperature to have a slow rise while the

physical temperature rises faster. In this case, the early-time radiance temperature very likely underestimates the physical temperature, whereas the late-time radiance temperature should converge closer to the physical value.

It is more difficult to determine the relationship between radiance temperature and physical temperature when the radiance comes from the reaction zone that forms after bubble collapse without a detonation (experiment 3). As Fig. 23 shows, the radiance temperatures of the various channels do not agree well even after we apply the correction for absorption in the unshocked NM. This lack of agreement suggests that the emissivity of the post-bubble collapse reaction zone may vary significantly with wavelength. Also, since the bubble initially under-fills the viewing area of the fiber, then grows with time while also being obscured by shocked NM, it is difficult to decouple changes in radiance from changes in the fraction of the light captured by the fiber. Thus, in the case of bubble collapse without detonation, the relationship between radiance temperature and physical temperature is unknown.

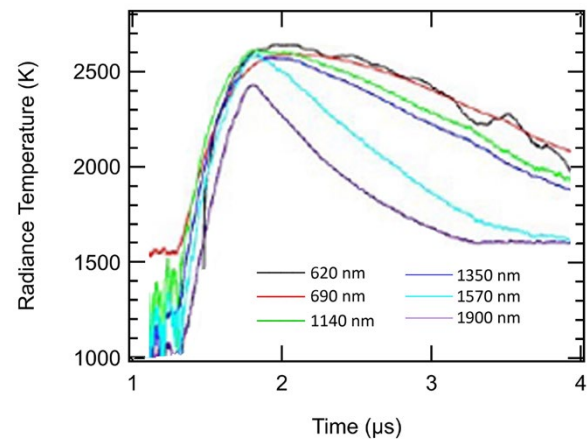


FIG. 23. Radiance temperature from six of the pyrometry channels for experiment 3, where bubble collapse is not followed by a sustained detonation. We observed large variances between the channels, probably because the emissivity varies substantially with wavelength in this case. Radiance for this experiment is primarily from the reaction zone that forms after the bubble collapses.

REFERENCES

- Aslam, T. D. 2018. "Shock temperature dependent rate law for plastic bonded explosives." *J. Appl. Phys.* **123**, 145901. <https://doi.org/10.1063/1.5020172>.
- Aslam, T. D., J. D. Bdzil, and L. B. Hill, "Extensions to DSD theory: Analysis of PBX 9502 rate stick data." in *Proceedings of the Eleventh International Symposium on Detonation* (Office of Naval Research, 1998) 1029–1037. <https://doi.org/10.2172/350869>.
- Aslam, T. D., D. M. Dattelbaum, J. A. Leiding, M. J. Cawkwell, C. Ticknor, S. A. Sheffield, and L. L. Gibson. 2024. "An Arrhenius-Wescott-Stewart-Davis (AWS) reactive flow model of nitromethane." *AIP Conf. Proc.* **3066**, 480001. <https://doi.org/10.1063/12.0028749>.

Effect of a collapsing gas bubble on the shock-to-detonation transition in liquid nitromethane

- Bourne, N. K., and J. E. Field. 1991. "Bubble collapse and the initiation of explosion." *Proc. R. Soc. Lond. A.* **435**, 423–435. <https://doi.org/10.1098/rspa.1991.0153>.
- Bourne, N. K., and J. E. Field. 1999. "Shock-induced collapse and luminescence by cavities." *Phil. Trans. R. Soc. A.* **357**, 295–311. <https://doi.org/10.1098/rsta.1999.0328>.
- Bourne, N. K., and A. M. Milne. "On cavity collapse and subsequent ignition." In *Proceedings of the Twelfth International Symposium on Detonation* (Office of Naval Research, 2002) 213–219. <https://citeseerx.ist.psu.edu/document?repid=rep1&type=pdf&doi=48d68e5276ad7c40e0d74a3a3be3f238d4104192>.
- Bourne, N. K., and A. M. Milne. 2003. "The temperature of a shock-collapsed cavity." *Proc. R. Soc. Lond. A.* **459**, 1851–1861. <https://doi.org/10.1098/rspa.2002.1101>.
- Chaiken, R. F. 1960. "Comments on hypervelocity wave phenomena in condensed explosives." *J. Chem. Phys.* **33**, 760–761. <https://doi.org/10.1063/1.1731254>.
- Flannigan, D. J., and K. S. Suslick. 2005. "Plasma formation and temperature measurement during single-bubble cavitation." *Nature* **434**, 52–55. <https://doi.org/10.1038/nature03361>.
- Handley, C. A., B. D. Lambourn, N. J. Whitworth, H. R. James, and W. J. Belfield. 2018. "Understanding the shock and detonation response of high explosives at the continuum and meso scales." *Appl. Phys. Rev.* **5**, 011303. <https://doi.org/10.1063/1.5005997>.
- Howe, P., R. Frey, B. Taylor, and V. Boyle. "Shock initiation and the critical energy concept." In *Proceedings of the Sixth International Symposium on Detonation* (Office of Naval Research, 1976) 11–19. <https://apps.dtic.mil/sti/tr/pdf/ADA059120.pdf>.
- Leiding, J. A., R. B. Jadrach, B. A. Lindquist, T. D. Aslam, and C. Ticknor. 2024. "Comparison of thermodynamic derivatives from DFT simulations and thermochemical calculations of PETN products." *AIP Conf. Proc.* **3066**, 510003. <https://doi.org/10.1063/12.0028671>.
- Lozano, E., M. J. Cawkwell, and T. D. Aslam. 2023. "An analytic and complete equation of state for condensed phase materials." *J. Appl. Phys.* **134**, 125102. <https://doi.org/10.1063/5.0165249>.
- Lysne, P. C., and D. R. Hardesty. 1973. "Fundamental equation of state of liquid nitromethane to 100 kbar." *J. Chem. Phys.* **59**, 6512–6523. <https://doi.org/10.1063/1.1680031>.
- Mercier, P., J. Bénier, P.A. Frugier, M. Debruyne, and B. Crouzet. 2010. "Nitromethane ignition observed with embedded PDV optical fibers." *EPJ Web Conf.* **10**, 00016. <https://doi.org/10.1051/epjconf/20101000016>.
- Michael, L., and N. Nikiforakis. 2019a. "The evolution of the temperature field during cavity collapse in liquid nitromethane. Part I: inert case." *Shock Waves* **29**, 153–172. <https://doi.org/10.1007/s00193-018-0802-8>.
- Michael, L., and N. Nikiforakis. 2019b. "The evolution of the temperature field during cavity collapse in liquid nitromethane. Part II: reactive case." *Shock Waves* **29**, 173–19. <https://doi.org/10.1007/s00193-018-0803-7>.
- Ticknor, C., S. A. Andrews, and J. A. Leiding. 2020. "Magpie: A new thermochemical code." *AIP Conf. Proc.* **2272**, 030033. <https://doi.org/10.1063/12.0000785>.
- Turley, W. D., B. M. La Lone, J. G. Mance, M. D. Staska, G. D. Stevens, L. R. Veaser, and D. M. Dattelbaum. 2021. "Experimental observations of shock-wave-induced bubble collapse and hot-spot formation in nitromethane liquid explosive." *J. Appl. Phys.* **129**, 145102. <https://doi.org/10.1063/5.0039414>.
- Winey, J. M., G. E. Duvall, M. D. Knudson, and Y. M. Gupta. 2000. "Equation of state and temperature measurements for shocked nitromethane." *J. Chem. Phys.* **113**, 7492–7501. <https://doi.org/10.1063/1.1312271>.